Mg modified LaTiO$_2$N with ameliorated photocarrier separation for solar water splitting

Guoan Lin [a,b], Xiaoqin Sun [a,b], Xiaoxiang Xu [a,b,*]

[a] *Clinical and Central Lab, Putuo People's Hospital, Tongji University, Shanghai 200060, China*
[b] *Shanghai Key Lab of Chemical Assessment and Sustainability, School of Chemical Science and Engineering, Tongji University, Shanghai, China*

ARTICLE INFO

ABSTRACT

LaTiO$_2$N is modified by Mg doping to construct solid solution series, i.e., LaTi$_{1-x}$Mg$_x$O$_{2+y}$N$_{1-y}$ ($0 \leq x \leq 0.5$). This modification effectively decreases the defect concentration (particularly bulk Ti^{3+} species and anion vacancies), increases the surface hydrophilicity, positively shifts the valence band top albeit it also enlarges the bandgap and induces Ti/Mg ordering when $x \geq 0.2$. These competitive tensions render an optimal composition at LaTi$_{0.9}$Mg$_{0.1}$O$_{2+y}$N$_{1-y}$ ($x = 0.1$) where both a low defect concentration and a disordered state of Ti/Mg can be reached, demonstrating much-improved photocarrier separation and exceptional photocatalytic activity with apparent quantum efficiency as high as 13.02 % at 420 ± 20 nm for O$_2$-evolution. Overall water splitting (H$_2$/O$_2$ molar ratio = 2/1) with good recycling stability has been realized by integrating LaTi$_{0.9}$Mg$_{0.1}$O$_{2+y}$N$_{1-y}$ into a Z-scheme system. These findings justify the efficacy of Mg as a useful modulator to improve the photocatalytic performance of metal oxynitrides.

1. Introduction

The prosperity of our modern economy is largely fertilized by fossil-fuel-based energy infrastructure, whose sustainability is severely jeopardized by the nonrenewable nature of the fossil fuels and various environmental issues related to their usage [1,2]. This has increasingly ignited the enthusiasm to develop clean energy techniques to decarbonize our energy infrastructure. In this context, photocatalytic water splitting has gained considerable interest as a simple and scalable technique to produce hydrogen - the ideal fuel for the future in a green and sustainable way [3–10]. After decades of efforts devoted to searching for photocatalytic materials, water can now be split efficiently over some wide-bandgap semiconductors irradiated by UV photons [3, 11]. However, it becomes rather difficult to do so based on narrow-bandgap semiconductors which can take advantage of most solar photons [12]. There are many competitive tensions, for instance, semiconductors with narrower bandgaps are accompanied by weaker photocarrier energetics [13]. Care has to be paid to expedite separation and transfer of the low energetic photocarriers since water splitting reactions are uphill reactions and involve multiple protons and charges.

As a typical narrow-bandgap semiconductor ($E_g \sim 2.0$ eV), LaTiO$_2$N warrants promising applications as a photocatalyst for solar water splitting. LaTiO$_2$N not only owns appropriate band edge positions relative to water redox potentials but also comprises earth-abundant elements favorable for large-scale manufacturing [14–17]. Despite these appealing properties, LaTiO$_2$N generally owns an unsatisfactory performance for photocatalytic water redox reactions [18,19]. This incongruous phenomenon is ascribed to a high concentration of defects generated at the synthetic stage, i.e. high-temperature ammonolysis [20]. In particular, Ti^{4+} has a relatively high electron-negativity thereby is susceptible to form Ti^{3+} defects which are known to undermine the photocatalytic activity [21]. Post-treatment of as-synthesized LaTiO$_2$N is useful to partially eliminate these defects, such as by calcining in the air or aqua regia etching [18,22]. Nevertheless, care has to be taken for these treatments in order to avoid the collapse of the LaTiO$_2$N structure [23]. Alternatively, aliovalent doping has shown great promise to inhibit defects in LaTiO$_2$N. Doping at La sublattice with some alkaline earth elements, e.g. La$_{1-x}$M$_x$TiO$_{2+y}$N$_{1-y}$ (M = Ca, Sr, and Ba), has witnessed a clear decrement of defect concentration and improved photocatalytic performance [19–21,24,25]. Considering a more direct linkage between the Ti sublattice and the electronic structure, it is of great interest to explore doping at the Ti sublattice of LaTiO$_2$N.

Previous studies have shown that Mg is a useful dopant for the modification of Nb- and Ta-based (oxy)nitrides [26,27]. The strong

inductive effects of Mg^{2+} help to inhibit the formation of defects and the presence of Mg at the surface is useful to increase surface hydrophilicity [28–30]. For instance, Mg dopants can effectively regulate the defect species in Ta_3N_5 and improve its surface properties such as wettability and cocatalyst deposition [31]. However, information is generally limited with regard to the change of a specific type of defects (e.g. bulk/surface defects, cation/anion defects, etc.) after Mg doping. Also the structural changes as a result of Mg incorporation and their impacts to the photocatalytic performance have not been adequately explored.

In this work, we have modified $LaTiO_2N$ by Mg doping to build solid solution series between $LaTiO_2N$ and $LaTi_{0.5}Mg_{0.5}O_3$, i.e. $LaTi_{1-x}Mg_xO_{2+y}N_{1-y}$ ($0 \leq x \leq 0.5$). The changes of different properties upon Mg incorporation, including the crystal structures and various types of defects, have been investigated to understand the optimal composition at $LaTi_{0.9}Mg_{0.1}O_{2+y}N_{1-y}$ which is characterized by the ameliorated photocarrier separation conditions and much-improved photocatalytic activity. As an exemplification for the practical application, $LaTi_{0.9}Mg_{0.1}O_{2+y}N_{1-y}$ is employed in a Z-scheme system which is capable of overall water splitting with good recycling stability under simulated solar insolation.

2. Experimental

2.1. Material synthesis

$LaTi_{1-x}Mg_xO_{2+y}N_{1-y}$ ($0 \leq x \leq 0.5$) was synthesized via a molten-salt assisted high-temperature ammonolysis of proper precursors. The precursors were prepared by a polymerized complex method[32]. Typically, for the precursor of $LaMg_{0.1}Ti_{0.9}O_{2.1}N_{0.9}$, 1.3463 g of titanium (IV) isopropoxide (Aladdin, 95 %), 0.1295 g $Mg(NO_3)_2 \cdot 6\ H_2O$ (SCR, 99 %), 2.1653 g $La(NO_3)_3 \cdot 9\ H_2O$ (Aladdin, 99 %) and 9.6540 g of anhydrous citric acid were added into 11.3 ml ethylene glycol under magnetic stirring. The transparent solution formed was then heated on a hotplate at 573 K for 2 h to produce a brown resin. The resin was then calcined in a muffle furnace at 823 K for 10 h to burn out the organic species. The resultant white powder was used as the precursor and was ground finely with NaCl (Aladdin, 99.5 %) and KCl (SCR, 99.8 %) in a molar ratio of 1:5:5. The mixtures were transferred into a tube furnace and heated at 1123 K for 5 h in flowing ammonia (Jiaya chemicals, 99.9999 %, 250 $ml \cdot min^{-1}$). The products were collected and rinsed repeatedly with deionized water to remove excess salts. The residues were then desiccated at 353 K overnight. The Mg content in the samples was varied by changing the initial $Mg(NO_3)_2 \cdot 6\ H_2O$ added. To construct a Z-scheme system, Rh doped $SrTiO_3$ was synthesized and was loaded with 0.5 wt% Ru cocatalyst following the literature [33].

2.2. Materials characterization

The X-ray powder diffraction (XRD) analysis was performed on an X-ray diffractometer (Bruker D8 Focus, Germany) with incident radiation of Cu $K_{\alpha 1}$ ($\lambda = 1.5406$ Å) and Cu $K_{\alpha 2}$ ($\lambda = 1.5444$ Å). Step size and duration of the signal collection were set as 0.5 s and 0.02°, respectively. Crystal structure parameters were determined by Rietveld refinements. The Raman spectra were collected on a Renishaw InVia Raman microscope (Renishaw, Wotton-under-Edge, UK), using green laser at 514 nm as the light source. The UV–vis diffuse reflectance spectra (UV–vis DRS) were acquired on a UV–vis spectrophotometer (JASCO-750, Japan). Sample powders were then inspected under microscopic conditions including a field emission scanning electron microscope (FE-SEM, Hitachi S4800, Japan) and a transmission electron microscopy (TEM, JEM-F200, Japan). Their surface states were also investigated by X-ray photoelectron spectroscopy (XPS, Thermo Escalab 250). The XPS data were referenced to the adventitious C 1s peak at 284.7 eV and were analyzed by XPSPEAK41 software for peak fit. The O and N content of different samples were examined using an oxygen-nitrogen-hydrogen (ONH) analyzer (ONH836, LECO Co., USA). Metal content (i.e., La,

Mg, Ti) of sample powders was analyzed using Laser Ablation Inductively Coupled Plasma Mass Spectrometry (LA-ICPMS, ICAP-TQ&NWR213, USA). The specific BET surface area was tested on a Micro-metrics instrument TriStar 3000. The dynamic water contact angle was analyzed by a wetting angle meter (Data Physics Instruments GmbH, Filderstadt, Germany). Before measurements, the sample powders (∼ 200 mg) were pressed into pellets which were polished by sandpapers (4000 mesh) to maintain a similar roughness. The pellets were then mounted onto a horizontal platform. About 50 μL distilled water were dropped onto the upper surface of the pellet. The whole process was recorded by a wetting angle meter (Data Physics Instruments GmbH, Filderstadt, Germany) equipped with a high-speed camera. Photoluminescence (PL) spectra were acquired using a spectrophotofluorometer (HORIBA FL-1016, Japan) at 77 K. Sample powders were excited by 420 nm photons. The electron paramagnetic resonance (EPR) spectra were collected on an X-band benchtop EPR spectrometer (EPR200M, CIQTEK, China). To get a better resolution on defects, the sample powders were cooled by a liquid nitrogen variable temperature system at 100 K during EPR measurements.

2.3. Photocatalytic water splitting

Photocatalytic experiments were performed in a top-illuminated quartz reactor combined with a closed circulation and evacuation system (Perfect Light, labsolar-6A). The reactor was wrapped with a water jacket to maintain the temperature at 293 K. For H_2-evolution experiments, Pt was loaded onto sample powders by impregnation method as a cocatalyst according to a previous report [34] and sodium sulfite was used as sacrificial agent. For O_2-evolution experiments, appropriate amounts of CoO_x were photo-deposited onto sample powders as a cocatalyst according to the previous reports [3,35]. In brief, 100 mg sample powders were dispersed into $Co(NO_3)_2$ aqueous solutions (7 mM) and were irradiated by full range illumination ($\lambda \geq 300$ nm) for 1 h. The product powders were recovered by centrifugation and were dried at 373 K. Silver nitrate (0.05 M) aqueous solution containing 0.2 g La_2O_3 was used as the sacrificial agent for O_2-evolution reactions. For a typical photocatalytic experiment, 100 mg sample powders loaded with cocatalyst were ultrasonically dispersed into 100 ml sacrificial agent solution. The suspensions were sealed in the reactor and were subject to evacuation for 45 min to remove air dissolved. A 300 W Xenon lamp filtered with a UV cut-off ($\lambda \geq 420$ nm) was used as the light source. The gas component within the reactor was monitored by an online gas chromatograph (GC, TECHCOMP-GC7900). The GC was equipped with a thermal conductivity detector and 5 Å molecular sieve columns and used ultrapure Ar as the carrier gas. The origin of oxygen during the O_2-evolution reactions was investigated by using $H_2^{18}O$ as a water source whose gas product was analyzed by gas chromatography-mass spectrometer (GC-MS, Thermo Scientific TRACE 1300). For Z-scheme overall water splitting, 50 mg CoO_x-loaded $LaTi_{1-x}Mg_xO_{2+y}N_{1-y}$ and 50 mg Ru-loaded Rh-doped $SrTiO_3$ were ultrasonically dispersed into $FeCl_3$ (2 mM) aqueous solutions. The pH of system was adjusted to 2.5 by using hydrochloric acid solutions. Simulated AM 1.5 G (100 $mW \cdot cm^{-2}$) was used as the light source and was produced by filtering a 300 W Xenon lamp with an AM 1.5 G filter. The experiment procedures were set the same as above. To assess the apparent quantum efficiency (AQE), monochromatic light was used as the light source which was produced by a bandpass filter over the Xenon lamp. A quantum meter (Apogee MP-300, USA) was used to determine the photon flux of each monochromatic light. The AQE was then calculated based on the following Eq. (1):

$$AQE = \frac{n \times moles\ of\ gas\ evolution\ per\ hour}{moles\ of\ photon\ flux\ per\ hour} \times 100\% \quad (1)$$

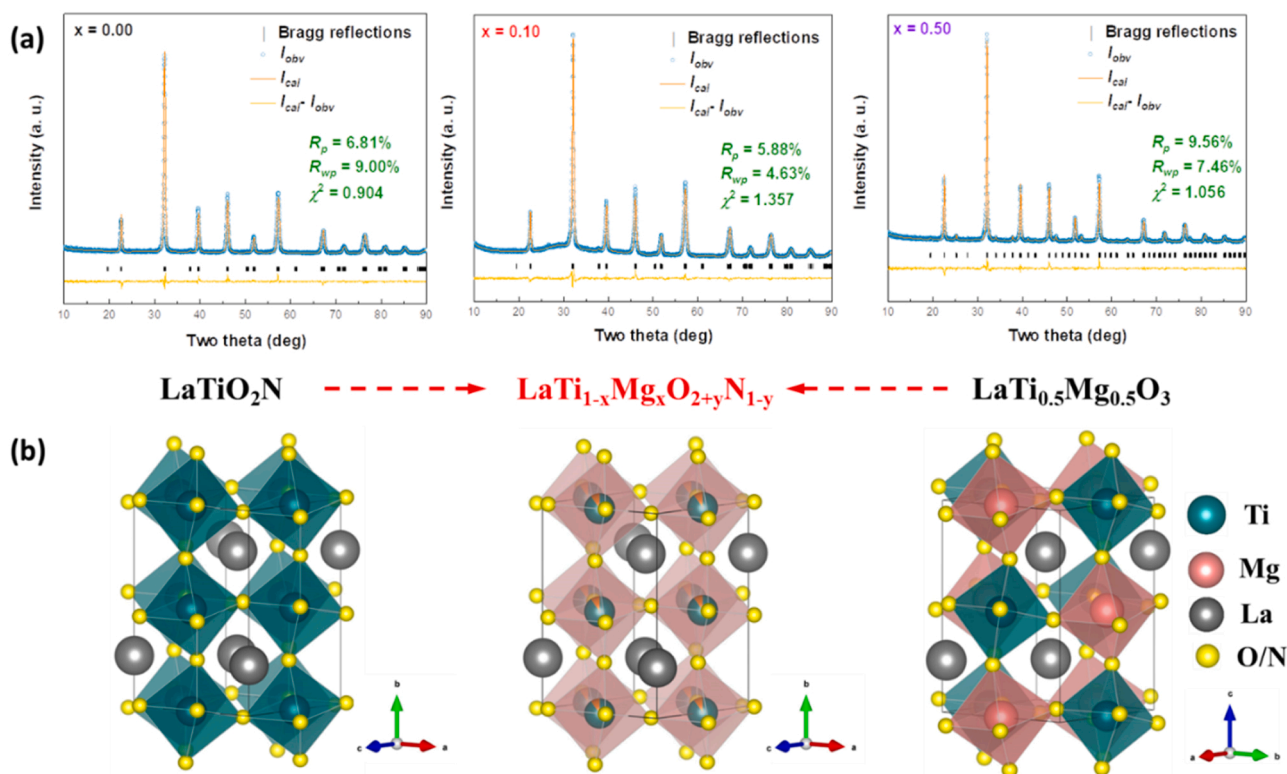where n = 2 and 4 for H_2 and O_2 evolution, respectively.

Fig. 1. (a) Observed and calculated XRD patterns for LaTiO$_2$N, LaTi$_{0.9}$Mg$_{0.1}$O$_{2+y}$N$_{1-y}$, and LaTi$_{0.5}$Mg$_{0.5}$O$_3$, the refinements all have good agreement factors as shown in the insets; (b) schematic illustration of the refined crystal structure of LaTiO$_2$N, LaTi$_{0.9}$Mg$_{0.1}$O$_{2+y}$N$_{1-y}$, and LaTi$_{0.5}$Mg$_{0.5}$O$_3$, their unit cells are marked by the black lines.

Table 1
Structure parameters, BET surface areas, and bandgap values of LaMg$_x$Ti$_{1-x}$O$_{2+y}$N$_{1-y}$ ($0 \leq x \leq 0.50$), standard deviations are included in the parentheses.

	Space group	a (Å)	b (Å)	c (Å)	β (°)	V (Å^3)	BET surface area (m^2/ g)	Band gap (eV)
x = 0.00	*Imma*	5.5673(3)	7.8761(6)	5.6054(3)	90.00(0)	245.79(2)	4.1(4)	2.11(1)
x = 0.10	*Imma*	5.5636(3)	7.8711(5)	5.6012(3)	90.00(0)	245.29(2)	3.5(2)	2.17(1)
x = 0.20	*P2$_1$/n*	5.5667(6)	5.5534(9)	7.8572(5)	90.18(9)	242.97(4)	7.9(7)	2.24(1)
x = 0.30	*P2$_1$/n*	5.5672(7)	5.5577(8)	7.8610(6)	90.05(1)	243.23(2)	10.5(5)	2.30(1)
x = 0.40	*P2$_1$/n*	5.5715(5)	5.5617(5)	7.8692(5)	90.04(1)	243.84(2)	7.0(4)	2.35(1)
x = 0.50	*P2$_1$/n*	5.5723(7)	5.5700(7)	7.8762(6)	90.06(6)	244.46(2)	2.8(2)	2.43(1)

2.4. Photoelectrochemical (PEC) analysis

The photoelectrodes of sample powders were fabricated according to our previous reports [36,37]. The PEC measurements were carried out using a three-electrode configuration comprising the photoelectrode, Pt foil, and Ag/AgCl as the working, counter, and reference electrode, respectively. Na$_2$SO$_4$ aqueous solution (pH = 7) was used as electrolyte. All electrodes were connected to a Zahner electrochemical workstation. Impedance spectra were collected by applying an AC signal of 1000 Hz to the photoelectrode at various potentials. Capacitance extracted from impedance spectra was used for Mott−Schottky analysis. The open circuit voltage decay (OCVD) experiments were performed in the Ar atmosphere following the procedure of a previous report [38].

2.5. Theoretical calculations

The electronic structures of LaTiO$_2$N, LaTi$_{0.9}$Mg$_{0.1}$O$_{2+y}$N$_{1-y}$, and LaTi$_{0.5}$Mg$_{0.5}$O$_3$ have been explored by theoretical calculations based on density functional theory (DFT). The calculations were performed using a commercial Vienna ab initio simulation package. For the calculation of LaTiO$_2$N, an orthorhombic unit cell ($a = 5.57$ Å, $b = 7.87$ Å, $c = 5.61$ Å, $\alpha = \beta = \gamma = 90°$) was built. However, for the calculation of

LaTi$_{0.9}$Mg$_{0.1}$O$_{2+y}$N$_{1-y}$, a $1 \times 2 \times 1$ supercell ($a = 5.57$ Å, $b = 15.74$ Å, $c = 5.61$ Å, $\alpha = \beta = \gamma = 90°$) was used instead. For the calculation of LaTi$_{0.5}$Mg$_{0.5}$O$_3$, a monoclinic unit cell ($a = 5.56$ Å, $b = 5.57$ Å, $c = 7.86$ Å, $\alpha = \gamma = 90°$, $\beta = 90.06°$) was built with Mg/Ti completely ordered at B-site. These structures were fully relaxed based on the criteria that every atom owns a force less than 0.01 eV·Å^{-1}. The calculations used generalized gradient approximation (GGA), Perdew-Burke-Ernzerhof (PBE) functional, and projector augmented wave pseudopotential. An energy cutoff of 500 eV was applied for static electric potential calculations. For geometry optimization, the total energy was set to be less than 10^{-5} eV.

3. Results and discussions

3.1. Crystal structure

Mg-doped LaTiO$_2$N, i.e. LaTi$_{1-x}$Mg$_x$O$_{2+y}$N$_{1-y}$ ($0 \leq x \leq 0.5$), can be considered as solid solutions series between LaTiO$_2$N and LaTi$_{0.5}$Mg$_{0.5}$O$_3$. Their structural correlations are illustrated in Fig. 1 which shows the Rietveld refinements of XRD data and the refined crystal structures. The LaTiO$_2$N (x = 0.0) crystallizes in an orthorhombic unit cell and can be described by a space group of *Imma* due to the anti-phase
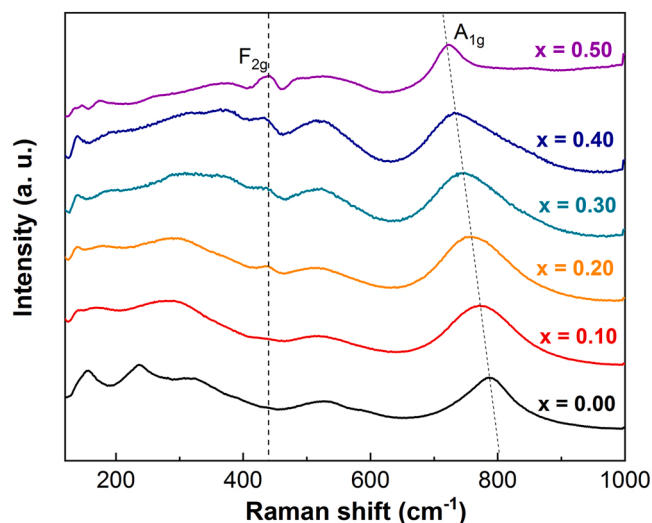
Fig. 2. Raman spectra of LaTi$_{1-x}$Mg$_x$O$_{2+y}$N$_{1-y}$ (0 ≤ x ≤ 0.5), dotted lines are the guides to the eye.

tilt of its Ti(O/N)$_6$ octahedrons in two directions (Glazer notation $a^-b^-c^0$) [39]. The LaTi$_{0.5}$Mg$_{0.5}$O$_3$ (x = 0.50), however, has a monoclinic unit cell and a space group of $P2_1/n$ as a result of octahedral tilting in three directions (Glazer notation $a^+b^-b^-$)[40]. The presence of (111) reflection around 25° indicates that Ti and Mg are ordered at the B sites of LaTi$_{0.5}$Mg$_{0.5}$O$_3$, as shown in the refined crystal structure (Fig. 1b)[41]. The solid solution series in between have crystal structures similar to either

LaTiO$_2$N or LaTi$_{0.5}$Mg$_{0.5}$O$_3$ with a watershed around x = 0.2 (Fig. S1 and Table 1). At regions below 0.1 (x ≤ 0.1), the solid solutions would maintain the structure of LaTiO$_2$N with disordered Ti and Mg at the Ti sublattice. A typical refined crystal structure of LaTi$_{0.9}$Mg$_{0.1}$O$_{2+y}$N$_{1-y}$ (x = 0.1) is shown in Fig. 1b which can be considered as the structure of LaTiO$_2$N superimposed with Ti/Mg disordering at Ti sublattice. For the region above 0.2 (x ≥ 0.2), Mg and Ti are segregated at the Ti sublattice and the structure undergoes more octahedral tilting as in the case of LaTi$_{0.5}$Mg$_{0.5}$O$_3$ (x = 0.50). This ordering/disordering phenomenon has also been verified by Raman spectra as shown in Fig. 2. The peak at 449 cm^{-1} is assignable to F$_{2g}$-like mode for a tilted perovskite which is correlated with B-site ordering [40]. Apparently, this peak is clearly resolved when x ≥ 0.2, indicating Ti/Mg ordering at Ti sublattice in these samples. The A$_{1g}$ mode at high wavenumbers (~ 800 cm^{-1}) is assignable to symmetric breathing of octahedral which is gradually red-shifted upon Mg incorporation [40]. This observation properly reflects the successive Mg incorporation which is accompanied by O/N substitution and statistically weakening of the Ti-O/N bond strength. It is noteworthy that the ordering of cations in perovskite is known to enlarge the bandgap when these cations have major contributions to the conduction band (CB) and valence band (VB) [42,43]. More importantly, cation ordering severely undermines photocarrier transport as it can narrow the conduction bandwidth according to the previous investigations [43,44]. Specifically, Ti/Mg ordering periodically breaks the three-dimensional -Ti-O/N-Ti-O/N-Ti- network in LaTiO$_2$N (i.e. -Ti-O/N-Mg-O/N-Ti-) which substantially hinders photocarrier transport (e.g. electrons in the Ti 3d-derived conduction band).

FE-SEM analysis suggests that all sample powders comprise irregular-shaped particles with particle size generally less than 200 nm
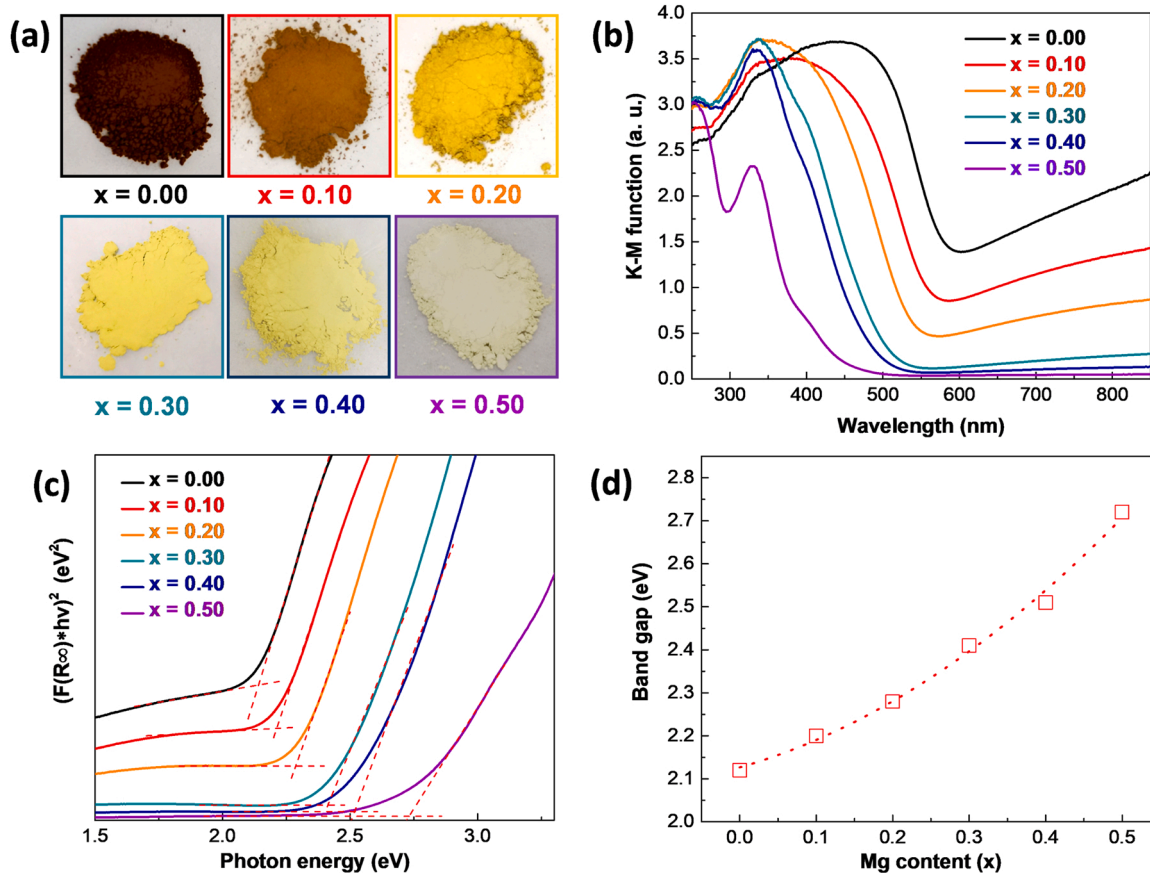

Fig. 3. (a) Digital photograph of LaTi$_{1-x}$Mg$_x$O$_{2+y}$N$_{1-y}$ (0 ≤ x ≤ 0.5) powders; (b) UV–vis DRS spectra of LaTi$_{1-x}$Mg$_x$O$_{2+y}$N$_{1-y}$ (0 ≤ x ≤ 0.5); (c) Tauc plot of LaTi$_{1-x}$Mg$_x$O$_{2+y}$N$_{1-y}$ (0 ≤ x ≤ 0.5), the direct bandgap is determined according to a previous report[45]; (d) Bandgap values of LaTi$_{1-x}$Mg$_x$O$_{2+y}$N$_{1-y}$ (0 ≤ x ≤ 0.5) as a function of Mg content.
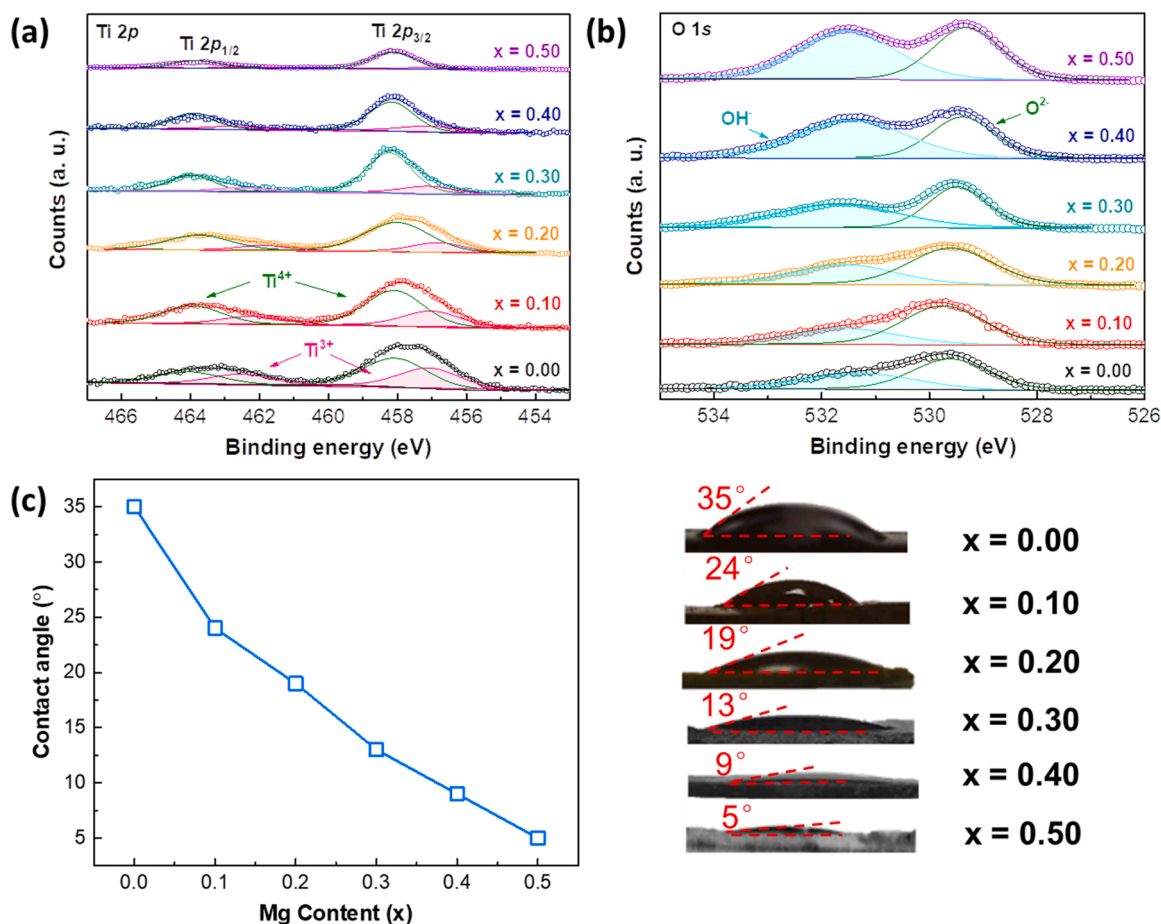
Fig. 4. (a) XPS Ti $2p$ spectra of LaTi$_{1-x}$Mg$_x$O$_{2+y}$N$_{1-y}$ ($0 \leq x \leq 0.5$); (b) XPS O $1s$ spectra of LaTi$_{1-x}$Mg$_x$O$_{2+y}$N$_{1-y}$ ($0 \leq x \leq 0.5$); (c) the water contact angle of LaTi$_{1-x}$Mg$_x$O$_{2+y}$N$_{1-y}$ ($0 \leq x \leq 0.5$).

(Fig. S2). There are clear variations in the particle size among different samples which are also properly reflected from their specific surface area summarized in Table 1. All elements are homogeneously dispersed within the sample particles according to SEM-EDS mapping analysis (Fig. S3), indicative of single-phase formation and uniform Mg doping. ICP-MS and ONH measurements reveal that the cation and anion content in the solid solutions are generally close to their stoichiometric values, confirming again the successful formation of solid solution series between LaTiO$_2$N and LaTi$_{0.5}$Mg$_{0.5}$O$_3$ (Table S1).

3.2. UV–vis light absorption

Although LaTi$_{1-x}$Mg$_x$O$_{2+y}$N$_{1-y}$ ($0 \leq x \leq 0.5$) powders have similar microstructures, they have distinct colors as shown by their digital photographs in Fig. 3a. Their colors change sequentially from dark red, brown, yellow, and light yellow to pale yellow along with Mg uptake, implying effective modulation of visible light absorption by Mg content. Fig. 3b compiles the UV–vis DRS spectra of LaTi$_{1-x}$Mg$_x$O$_{2+y}$N$_{1-y}$ ($0 \leq x \leq 0.5$) powders. Being consistent with the previous report[18], the spectra of LaTiO$_2$N ($x = 0.0$) are characterized by a clear absorption edge (~ 600 nm) superimposed by an intensive post-edge absorption tail that extends deeply into the infrared region. The post-edge absorption tail typically belongs to transitions associated with midgap defect levels and is responsible for the dark hue of the sample colors [46–48]. Upon Mg doping, the absorption edge is consecutively blue-shifted whilst the post-edge absorption tail is quickly damped, indicating that Mg doping enlarges the bandgap and scavenges the defects. The former can be rationalized by the fact that Mg doping is accompanied by a decrease in N content which contributes mostly to the top of VB [18]. The bandgap

values of LaTi$_{1-x}$Mg$_x$O$_{2+y}$N$_{1-y}$ ($0 \leq x \leq 0.5$) are determined by the Tauc plot method (Fig. 3c) following a previous report [45]. The bandgap increases monotonically along with Mg content in the solid solutions (Fig. 3d), suggesting that Mg dopants are effective modulators to precisely control the absorption threshold. It is noteworthy that the curve in Fig. 3d shows a clear nonlinear trend at high Mg content ($x \geq 0.3$). The accelerated bandgap enlargement at this region can be attributed to the Ti/Mg ordering in the Ti sublattice which weakens the orbital hybridizations and narrows the bandwidth [49], e.g., between adjacent Ti $3d$ orbitals, etc.

3.3. Surface state

We continue to investigate the surface state of LaTi$_{1-x}$Mg$_x$O$_{2+y}$N$_{1-y}$ ($0 \leq x \leq 0.5$) employing XPS analysis and water contact angle measurements. Fig. 4a compiles the XPS Ti $2p$ spectra of LaTi$_{1-x}$Mg$_x$O$_{2+y}$N$_{1-y}$ ($0 \leq x \leq 0.5$). The overlapping peaks are unfolded and properly fitted as summarized in Table S2. The Ti $2p$ spectra of LaTiO$_2$N ($x = 0.0$) are represented by two distinct spin-orbit-split pairs assignable to Ti^{3+} and Ti^{4+} species as marked in Fig. 4a [20,21]. The comparable peak area of Ti^{3+} and Ti^{4+} species is consistent with UV–vis DRS spectra that LaTiO$_2$N is rich in defects. Quite strikingly, the peaks of Ti^{3+} species are gradually decreased after Mg doping and are almost absent in the case of $x = 0.50$. This observation in line with UV–vis DRS spectra confirms that Mg doping indeed inhibits defect formation. Moreover, the XPS O $1s$ spectra contain two overlapping peaks for all samples (Table S3). The one at low binding energy side (~ 529.5 eV) can be assigned to lattice oxygen (O^{2-}) whilst the one at high binding energy side (~ 531.5 eV) belongs to surface hydroxyl groups (OH$^-$) [50,51].
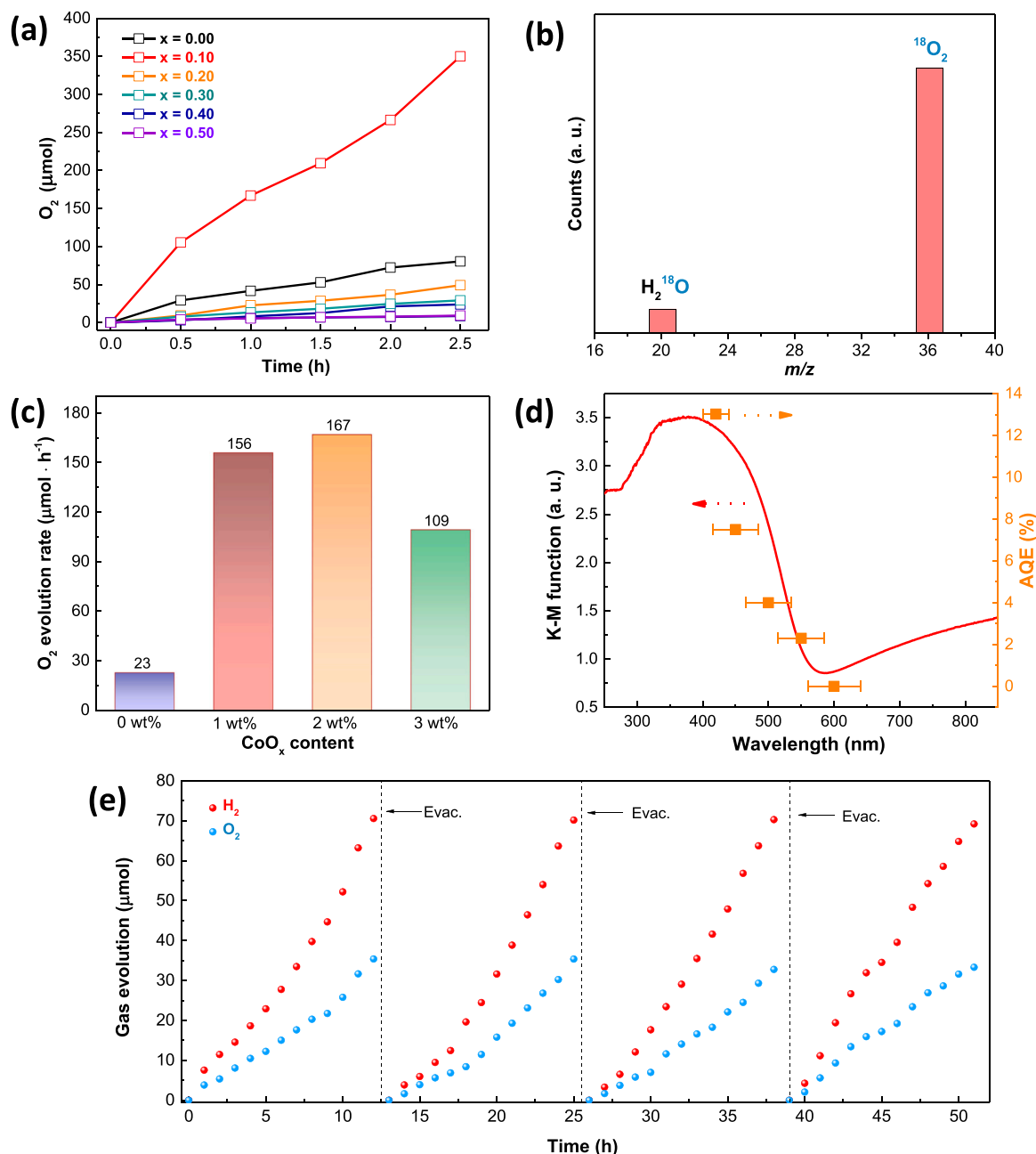
Fig. 5. (a) Photocatalytic O_2-evolution of $LaTi_{1-x}Mg_xO_{2+y}N_{1-y}$ ($0 \leq x \leq 0.5$) as a function of time under visible light illumination ($\lambda \geq 420$ nm); (b) mass spectra of gaseous product over $LaTi_{0.9}Mg_{0.1}O_{2+y}N_{1-y}$ in the presence of $H_2^{18}O$ and visible light illumination ($\lambda \geq 420$ nm); (c) average O_2-evolution rate over $LaTi_{0.9}Mg_{0.1}O_{2+y}N_{1-y}$ as a function of CoO_x content; (d) action spectra of $LaTi_{0.9}Mg_{0.1}O_{2+y}N_{1-y}$, UV–vis DRS spectra are also included for comparisons; (e) overall water splitting over a Z-scheme system comprising $LaTi_{0.9}Mg_{0.1}O_{2+y}N_{1-y}$ (loaded with 2 wt% CoO_x), $SrTiO_3$:Rh (loaded with 1 wt% Ru), and Fe^{2+}/Fe^{3+} redox mediator (2 mM), the system was illuminated by simulated AM 1.5 G and was evacuated every 12 h.

Apparently, the surface hydroxyl groups are clearly increased along with Mg doping, indicating that $LaTiO_2N$ becomes more hydrophilic after Mg modifications. This deduction is further confirmed by the water contact angle measurements (Fig. 4c) [30]. The water contact angle decreases rapidly along with Mg doping from 35° ($x = 0.0$) to 5° ($x = 0.5$), affirming the increased surface hydrophilicity. Hydroxyl groups play a crucial role in water redox reactions thereby a hydrophilic surface is beneficial for a water-splitting photocatalyst [52,53]. The XPS spectra of the survey scan and other constituent elements, i.e., N 1 *s*, Mg 1 *s* and La 3*d* states are compiled in Fig. S4. These spectra are generally consistent with the element content in $LaTi_{1-x}Mg_xO_{2+y}N_{1-y}$ ($0 \leq x \leq 0.5$) and show similar binding energy state for all samples.

3.4. Photocatalytic activity

The O_2-evolution reactions are considered to be the rate-limiting steps for overall water splitting reactions [54]. The photocatalytic performance of $LaTi_{1-x}Mg_xO_{2+y}N_{1-y}$ ($0 \leq x \leq 0.5$) is accessed by comparing their O_2-evolution under visible light illumination ($\lambda \geq 420$ nm). The O_2-evolution reactions have been accelerated by using $AgNO_3$ aqueous solution as a sacrificial agent and CoO_x as a cocatalyst. Spontaneous O_2-evolution reactions that do not proceed photocatalytically are excluded by a series of control experiments that lack one of the following components, e.g. photocatalyst, light, water, *etc*. The temporal O_2-evolution of all samples is illustrated in Fig. 5a. It can be seen from Fig. 5a that the photocatalytic activity of
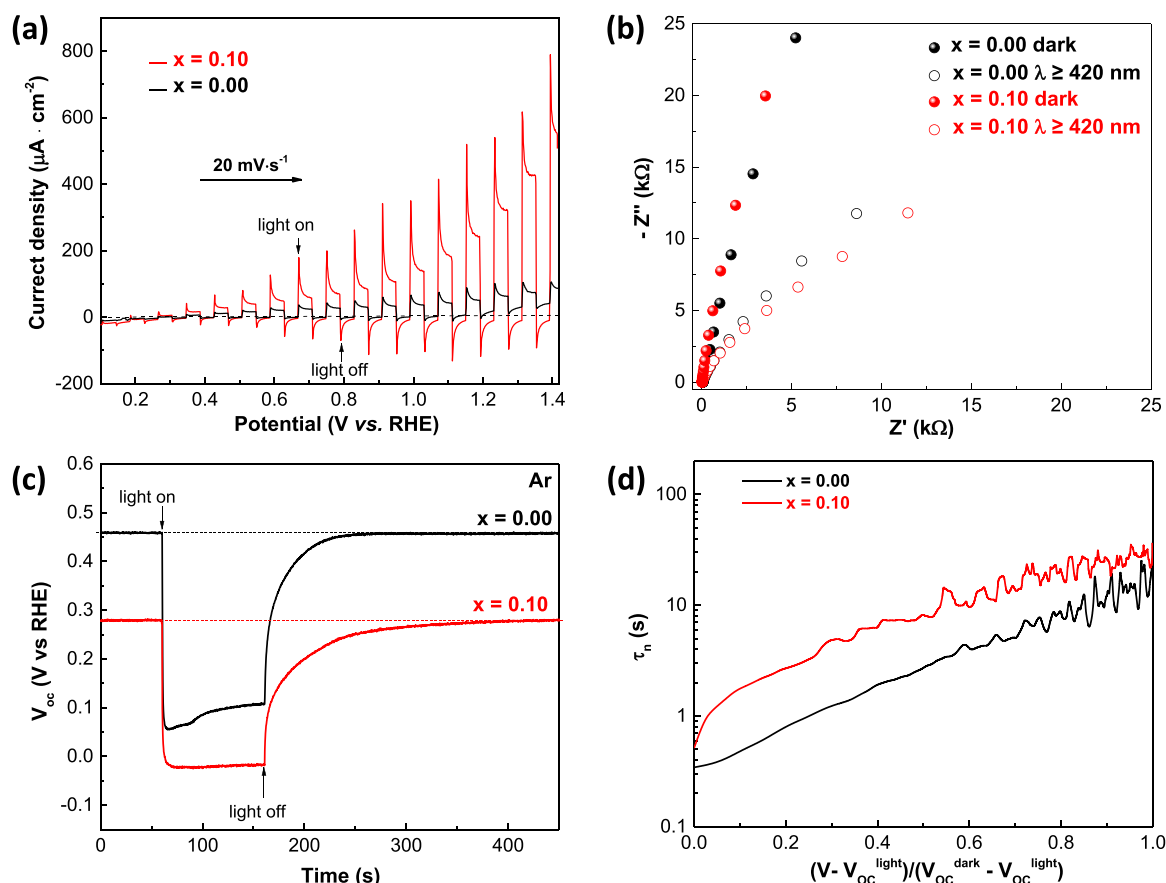
Fig. 6. (a) LSV of $LaTiO_2N$ and $LaTi_{0.9}Mg_{0.1}O_{2+y}N_{1-y}$ under chopped visible light illumination ($\lambda \geq 420$ nm); (b) Nyquist plot of electrochemical impedance spectra of $LaTiO_2N$ and $LaTi_{0.9}Mg_{0.1}O_{2+y}N_{1-y}$; (c) open-circuit voltage decay (OCVD) profile of $LaTiO_2N$ and $LaTi_{0.9}Mg_{0.1}O_{2+y}N_{1-y}$ in Ar; (d) the OCVD lifetime for $LaTiO_2N$ and $LaTi_{0.9}Mg_{0.1}O_{2+y}N_{1-y}$.
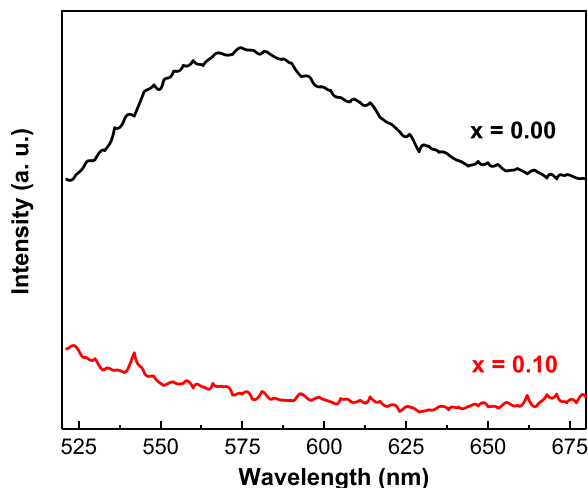

Fig. 7. Photoluminescence spectra of $LaTiO_2N$ and $LaTi_{0.9}Mg_{0.1}O_{2+y}N_{1-y}$.

$LaTi_{1-x}Mg_xO_{2+y}N_{1-y}$ ($0 \leq x \leq 0.5$) shows a volcano-type relation to the Mg content in the structure. Specifically, the activity increases dramatically after Mg doping and decreases quickly at higher Mg doping levels. Similar trend is also observed for photocatalytic H_2-evolution reactions although the activity is much-lower (Fig. S5). In both cases, the $LaTi_{0.9}Mg_{0.1}O_{2+y}N_{1-y}$ ($x = 0.1$) delivers the highest activity which has a 4.4-fold enhancement in O_2-evolution and 3-fold enhancement in H_2-evolution compared to pristine $LaTiO_2N$. The origin of its

O_2-evolution is confirmed by water oxidation from a control experiment using $H_2^{18}O$ as the water resource (Fig. 5b). The amounts of CoO_x loaded are further adjusted to maximize the photocatalytic activity of $LaTi_{0.9}Mg_{0.1}O_{2+y}N_{1-y}$ (Fig. 5c, Table S4). 2 wt% CoO_x is found to give the optimal performance. The CoO_x cocatalyst is intimately anchored at the surface of $LaTi_{0.9}Mg_{0.1}O_{2+y}N_{1-y}$ according to TEM inspections (Fig. S6). The action spectra were then collected under the optimal cocatalyst loading point. The action spectra are displayed in Fig. 4d which illustrates the apparent quantum efficiency (AQE) as a function of photon wavelength. The AQE has an onset wavelength around 600 nm and follows the UV–vis DRS spectra. Therefore, O_2-evolution over $LaTi_{0.9}Mg_{0.1}O_{2+y}N_{1-y}$ is essentially photon-driven and is activated by bandgap excitations. With the aid of CoO_x cocatalyst, $LaTi_{0.9}Mg_{0.1}O_{2+y}N_{1-y}$ achieves an AQE as high as 13.02 % at 420 ± 20 nm for water oxidation into O_2, outperforming most $LaTiO_2N$-based photocatalysts reported (Table S5). XRD, SEM and N content analysis confirm the good stability of $LaTi_{0.9}Mg_{0.1}O_{2+y}N_{1-y}$ for water oxidation reactions (Fig. S7 and Table S6). Given the superior activity for O_2-evolution, we have fabricated a Z-scheme system employing $LaTi_{0.9}Mg_{0.1}O_{2+y}N_{1-y}$ as the O_2-evolution moiety. Under simulated AM 1.5G illumination, the as-prepared Z-scheme system is capable of overall water splitting with a correct H_2/O_2 ratio and good recycling stability (Fig. 5e), warranting promising applications for solar water splitting. The calculated AQE for Z-scheme overall water splitting achieves 0.11 % at 420 ± 20 nm (Fig. S8).

3.5. Photocarrier separation

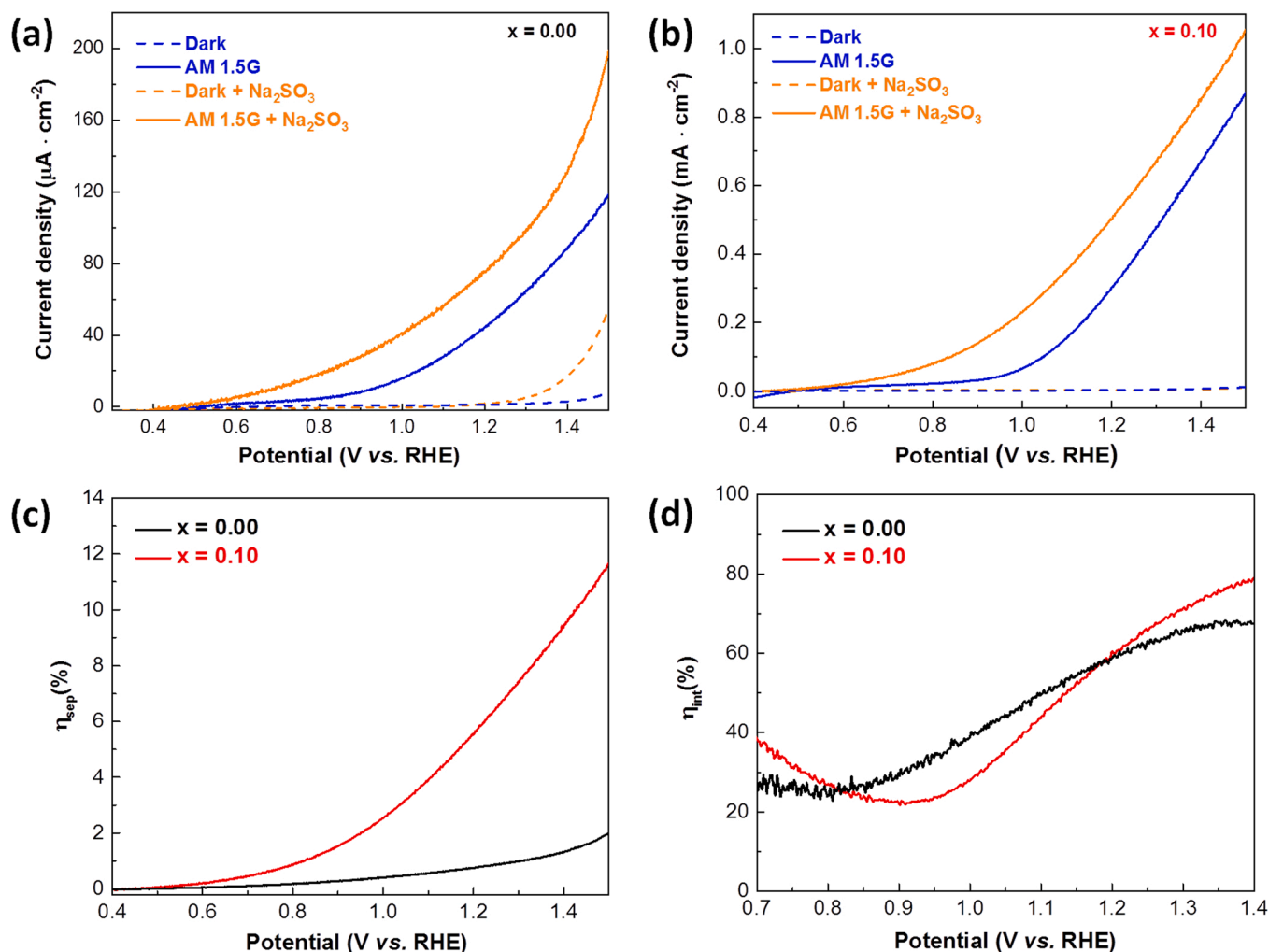To elucidate the distinct photocatalytic activity, the photocarrier

Fig. 8. (a) Linear sweep voltammetry of LaTiO₂N in dark or under simulated AM 1.5G illuminations with or without Na₂SO₃; (b) Linear sweep voltammetry of LaTi$_{0.9}$Mg$_{0.1}$O$_{2+y}$N$_{1-y}$ in dark or under simulated AM 1.5G illuminations with or without Na₂SO₃; (c) charge separation efficiency of LaTiO₂N and LaTi$_{0.9}$Mg$_{0.1}$O$_{2+y}$N$_{1-y}$; (c) interfacial charge transfer efficiency of LaTiO₂N and LaTi$_{0.9}$Mg$_{0.1}$O$_{2+y}$N$_{1-y}$.
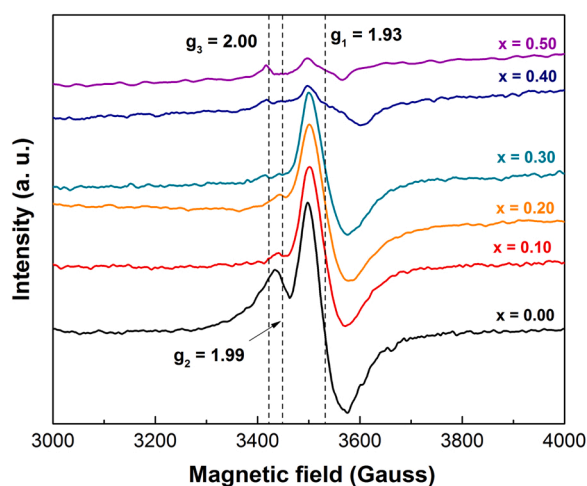

Fig. 9. The electron paramagnet resonance (EPR) spectra of LaTi$_{1-x}$Mg$_x$O$_{2+y}$N$_{1-y}$ ($0 \leq x \leq 0.5$) at 100 K.

separation conditions in LaTiO₂N and LaTi$_{0.9}$Mg$_{0.1}$O$_{2+y}$N$_{1-y}$ are explored. Firstly, photoelectrochemical analysis was performed using photoelectrodes fabricated by sample powders. Fig. 6a shows the linear

sweep voltammetry (LSV) of photoelectrodes illuminated by a chopped visible light beam ($\lambda \geq 420$ nm). Under the same electrical bias, LaTi$_{0.9}$Mg$_{0.1}$O$_{2+y}$N$_{1-y}$ clearly gives a much-higher photocurrent than LaTiO₂N. On the other hand, electrochemical impedance spectra (EIS) reveal that LaTi$_{0.9}$Mg$_{0.1}$O$_{2+y}$N$_{1-y}$ owns a comparable interfacial charge transfer resistance with LaTiO₂N (Fig. 6b). These results jointly suggest that LaTi$_{0.9}$Mg$_{0.1}$O$_{2+y}$N$_{1-y}$ has better photocarrier separation conditions than LaTiO₂N and is consistent with the high photocatalytic activity observed. This deduction is also verified by open-circuit voltage decay (OCVD) experiments (Fig. 6c)[55]. The decay of open-circuit voltage (V_{oc}) after light termination is directly linked to the dissipation of photocarriers (e.g. recombination) thereby properly reflecting the photocarrier separation conditions in the semiconductor [56]. After 100 s of light illumination, it takes about 90 s for pristine LaTiO₂N to restore its open-circuit voltage (V_{oc}) back to the value in the dark. However, it takes a considerably longer time (260 s) for LaTi$_{0.9}$Mg$_{0.1}$O$_{2+y}$N$_{1-y}$ to do so. The corresponding OCVD lifetime is illustrated in Fig. 6d which clearly reveals LaTi$_{0.9}$Mg$_{0.1}$O$_{2+y}$N$_{1-y}$ has more long-lived photocarriers than LaTiO₂N. Secondly, the radiation-type photocarrier recombination has been probed by photoluminescence (PL) spectra (Fig. 7). The PL spectra of LaTiO₂N are characterized by a broad peak whose summit lies close to 580 nm, corresponding to the band edge emission (~ 2.1 eV). However, such PL signal is completely damped in LaTi$_{0.9}$Mg$_{0.1}$O$_{2+y}$N$_{1-y}$, suggesting that the photocarriers are promptly
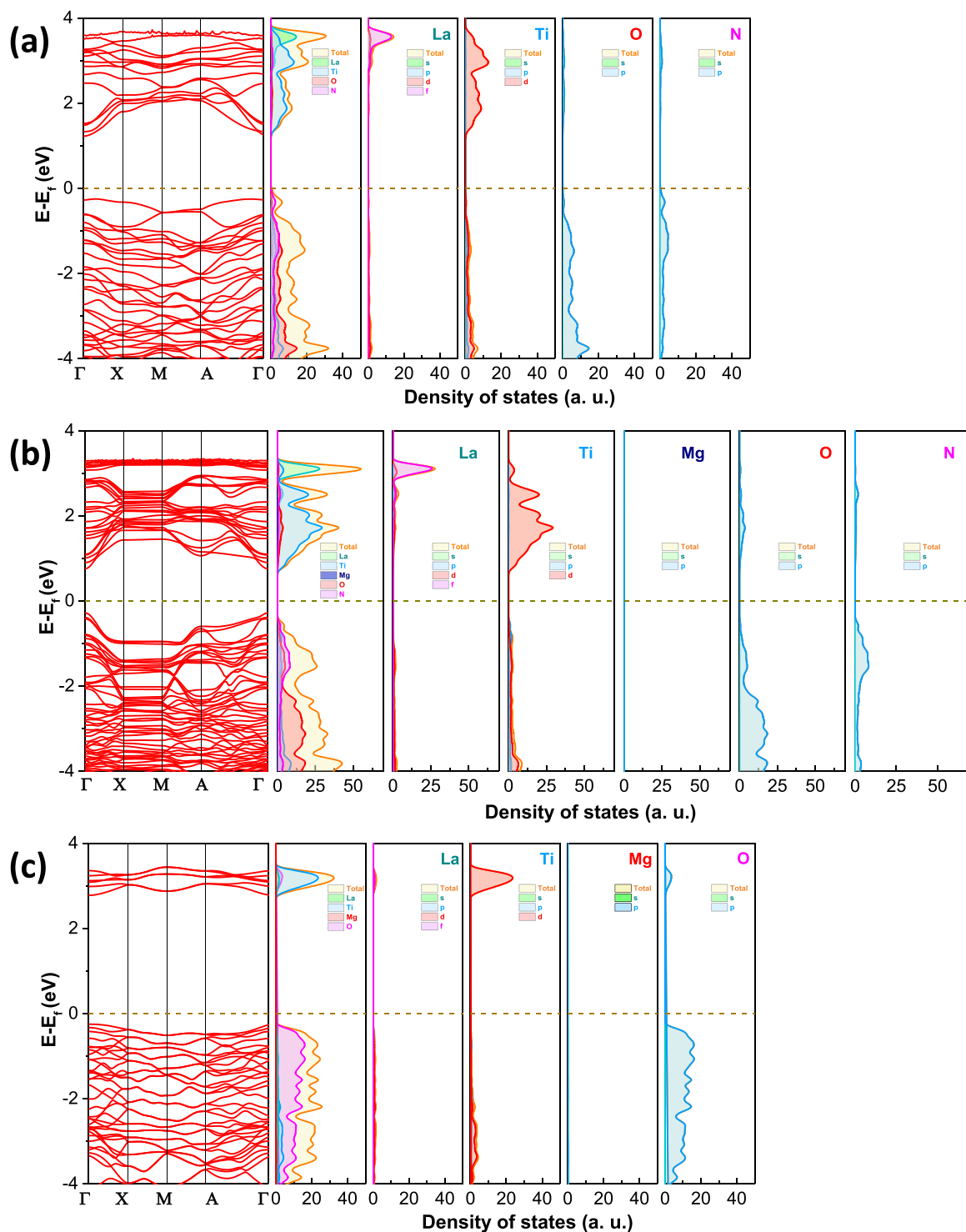
Fig. 10. Band structure, density of states (DOS) and projected density of states (PDOS) for (a) $LaTiO_2N$; (b) $LaTi_{0.9}Mg_{0.1}O_{2+y}N_{1-y}$; (c) $LaTi_{0.5}Mg_{0.5}O_3$.

dissociated [57]. Moreover, the photocarrier separation efficiency is further quantified with an aid of Na_2SO_3 during LSV measurements. According to a previous report [58], the photocurrent density is governed by the following equation (Eq. 2):

$$J = J_{abs} \times \eta_{sep} \times \eta_{int} \qquad (2)$$

where J_{abs}, η_{sep}, and η_{int} are photon absorption efficiency, charge separation efficiency, and interfacial charge transfer efficiency, respectively. The J_{abs} is calculated to be 9.04 and 9.21 mA·cm^2 for pristine $LaTiO_2N$

and $LaTi_{0.9}Mg_{0.1}O_{2+y}N_{1-y}$, respectively (Fig. S9). When Na_2SO_3 is used during PEC measurements, the fast sulfite oxidation kinetics ensures that η_{int} is almost 100%. The η_{sep} can then be deduced by dividing the measured photocurrent ($J_{NaOH+Na_2SO_3}$) with J_{abs}. Likewise, the η_{int} can be determined by dividing J_{NaOH} with $J_{NaOH+Na_2SO_3}$ [59]. Consistently with the previous analysis, $LaTi_{0.9}Mg_{0.1}O_{2+y}N_{1-y}$ owns a much-higher charge separation efficiency than $LaTiO_2N$ while their interfacial charge transfer efficiency is close (Fig. 8c-d).
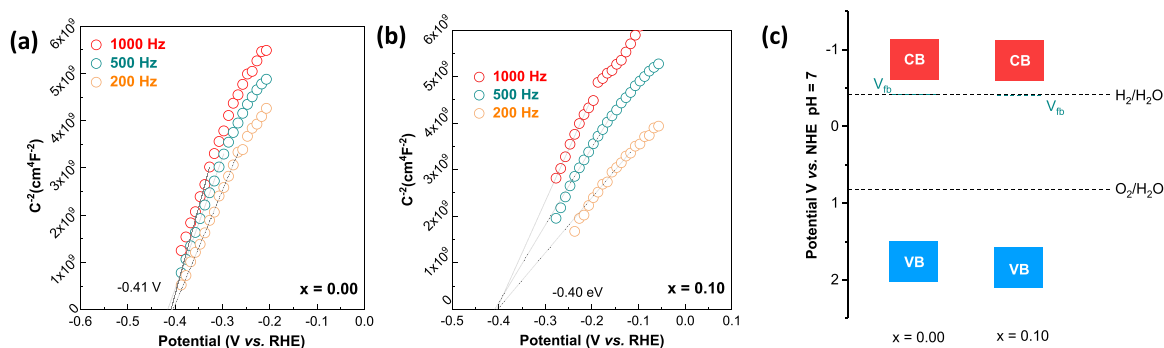
Fig. 11. (a) Mott-Schottky plot of $LaTiO_2N$ at different frequencies; (b) Mott-Schottky plot of $LaTi_{0.9}Mg_{0.1}O_{2+y}N_{1-y}$ at different frequencies; (c) schematic illustration of band edge positions of $LaTiO_2N$ and $LaTi_{0.9}Mg_{0.1}O_{2+y}N_{1-y}$.

3.6. Electron paramagnetic resonance spectra (EPR)

An intuitive question arises as why the optimal composition lies at x = 0.1 which also has a high defect concentration according to XPS analysis (Fig. 4a). Since XPS analysis is limited to the sample surface, we have performed low temperature EPR analysis to distinguish different types of defects (e.g. bulk and surface ones, cation and anion ones, etc.) and their changes upon Mg incorporation. Fig. 9 illustrate EPR spectra of all samples at 100 K in which three EPR signals with distinct g values can be identified, i.e. $g_1 \sim 1.93$, $g_2 \sim 1.99$, and $g_3 \sim 2.00$, corresponding to surface Ti^{3+}, bulk Ti^{3+}, and oxygen/nitrogen vacancies, respectively [60–63]. Compared to pristine $LaTiO_2N$, the surface Ti^{3+} EPR signal ($g_1 \sim 1.93$) remains high up to x = 0.3, being consistent with XPS results that these samples contains a high concentration of surface Ti^{3+} defects (Fig. 4a). On the contrary, a quick damp of the EPR signal for the bulk Ti^{3+} ($g_2 \sim 1.99$) and oxygen/nitrogen vacancies ($g_3 \sim 2.00$) can be seen upon Mg incorporation, indicating that Mg dopants are more efficient annihilators for these defects. This helps to explain the improved photocarrier separation conditions in $LaTi_{0.9}Mg_{0.1}O_{2+y}N_{1-y}$ as bulk Ti^{3+} and oxygen/nitrogen vacancies are electronically active trapping centers for photocarriers, e.g. holes being trapped by bulk Ti^{3+} and electrons being trapped by oxygen/nitrogen vacancies. Nevertheless, the benefit of the defect annihilation can be substantially counteracted by Ti/Mg ordering which occurs when x ≥ 0.2. Ti/Mg ordering periodically breaks the three-dimensional -Ti-O/N-Ti-O/N-Ti- network in $LaTiO_2N$ (i. e., -Ti-O/N-Mg-O/N-Ti-) therefore inhibiting photocarrier transport (e. g., electrons in the Ti 3d-derived conduction band). The optimal composition at x = 0.1 for the highest photocatalytic activity is most probably because it not only has a low concentration of defects (e.g., bulk Ti^{3+} and oxygen/nitrogen vacancies) but also maintains a disordering state for Ti/Mg at Ti sublattice. The change of other properties such as surface hydrophilicity and bandgap upon Mg incorporation may also contribute to the modulation of the photocatalytic activity but probably to a less extent.

3.7. Band structure

The band structure of $LaTi_{0.9}Mg_{0.1}O_{2+y}N_{1-y}$ and its parent compound $LaTiO_2N$ and $LaTi_{0.5}Mg_{0.5}O_3$ are further investigated to understand the impact of Mg and Ti/Mg ordering on the electronic structures. Fig. 10 illustrates their calculated band structure, density of states (DOS) and projected density of states (PDOS) based on DFT. All samples are essentially semiconductors with bandgap values calculated to be 0.89 eV, 1.03 eV, and 3.03 eV for $LaTiO_2N$, $LaTi_{0.9}Mg_{0.1}O_{2+y}N_{1-y}$, and $LaTi_{0.5}Mg_{0.5}O_3$, respectively. Thereby, Mg doping indeed enlarges the bandgap. The deviation of bandgap values relative to experimental ones are commonly encountered for GGA method [64]. Their band structures close to Fermi levels are dominated by Ti and O/N atoms, as revealed by DOS analysis. More specifically, the CB is mainly contributed by Ti 3d

orbitals whilst the VB is formed by the hybridization of O 2p/N 2p orbitals. Although Mg does not participate directly in the formation CB and VB, it serves as a modulator to tune O/N ratio which modifies the position of VB. More importantly, the conduction bandwidth is significantly narrowed when Ti/Mg ordering occurs as in the case of $LaTi_{0.5}Mg_{0.5}O_3$ (Fig. 10c). A narrowed conduction bandwidth typically contributes to poor electron mobility and prevents fast electron transport, being unfavorable for the separation of photocarriers. These results agree well with previous analysis on the role of Mg dopants. On the other hand, flat band potential of $LaTiO_2N$ and $LaTi_{0.9}Mg_{0.1}O_{2+y}N_{1-y}$ is determined to be − 0.41 V and − 0.40 V vs RHE by Mott-Schottky (MS) analysis (Fig. 11a and b). Assuming that CB edge is 0.2 V more negative than the flat band potential [65,66], the band edge positions of both compounds can be roughly deduced considering their bandgaps and are depicted schematically in Fig. 11c. Being consistent with DFT calculations, VB edge is positively shifted by Mg doping which is beneficial for water oxidation reactions since holes will have a stronger oxidative force.

4. Conclusions

Solid solution series between $LaTiO_2N$ and $LaTi_{0.5}Mg_{0.5}O_3$, i.e. $LaTi_{1-x}Mg_xO_{2+y}N_{1-y}$ (0 ≤ x ≤ 0.5), have been investigated as the photocatalysts for water oxidation reactions. These solid solutions maintain the crystal structure of their parent compounds with a structural transformation around x = 0.1. The Mg dopants at the Ti sublattice undergo a disordering to ordering transition across the watershed. Mg doping not only enlarges the bandgap of $LaTiO_2N$ and narrows conduction bandwidth when Ti/Mg ordering occurs but also effectively decreases the defect concentration (particularly bulk Ti^{3+} species and oxygen/nitrogen vacancies), increases the surface hydrophilicity, and positively shifts the VB edge. These competitive tensions result in an optimal composition at $LaTi_{0.9}Mg_{0.1}O_{2+y}N_{1-y}$ where both a low defect concentration and Mg/Ti structural disordering can be reached, delivering exceptional photocatalytic activity. When loaded with proper amounts of CoO_x cocatalyst, $LaTi_{0.9}Mg_{0.1}O_{2+y}N_{1-y}$ achieves an AQE as high as 13.02 % at 420 ± 20 nm for O_2-evolution, surpassing most $LaTiO_2N$-based photocatalysts reported. A Z-scheme system employing $LaTi_{0.9}Mg_{0.1}O_{2+y}N_{1-y}$ as the O_2-evolution moiety shows stable activity for overall water splitting with correct stoichiometry. These findings provide a paradigm to improve the photocatalytic performance of oxynitrides by aliovalent doping.

CRediT authorship contribution statement

Guoan Lin: Investigation, Methodology, and Data curation; **Xiaoqin Sun**: Formal analysis, Investigation; **Xiaoxiang Xu**: Funding acquisition, Project administration, Resources, Software, Supervision, Validation, Writing – original draft, Writing – reviewing & editing.

Declaration of Competing Interest

The authors declare that they have no known competing financial interests or personal relationships that could have appeared to influence the work reported in this paper.

Data availability

Data will be made available on request.

Acknowledgments

Appendix A. Supporting information

Supplementary data associated with this article can be found in the online version at doi:10.1016/j.apcatb.2022.122258.

References

[1] N.S. Lewis, D.G. Nocera, Powering the planet: chemical challenges in solar energy utilization, Proc. Natl. Acad. Sci. USA 103 (2006) 15729–15735, https://doi.org/10.1073/pnas.0603395103.

[2] D.G. Nocera, Living healthy on a dying planet, Chem. Soc. Rev. 38 (2009) 13–15, https://doi.org/10.1039/b820660k.

[3] T. Takata, J.Z. Jiang, Y. Sakata, M. Nakabayashi, N. Shibata, V. Nandal, K. Seki, T. Hisatomi, K. Domen, Photocatalytic water splitting with a quantum efficiency of almost unity, Nature 581 (2020) 411–414, https://doi.org/10.1038/s41586-020-2278-9.

[4] H. Nishiyama, T. Yamada, M. Nakabayashi, Y. Maehara, M. Yamaguchi, Y. Kuromiya, Y. Nagatsuma, H. Tokudome, S. Akiyama, T. Watanabe, R. Narushima, S. Okunaka, N. Shibata, T. Takata, T. Hisatomi, K. Domen, Photocatalytic solar hydrogen production from water on a 100m² scale, Nature 598 (2021) 304–307, https://doi.org/10.1038/s41586-021-03907-3.

[5] X.X. Xu, C. Randorn, P. Efstathiou, J.T.S. Irvine, A red metallic oxide photocatalyst, Nat. Mater. 11 (2012) 595–598, https://doi.org/10.1038/Nmat3312.

[6] L. Yang, Q.Y. Fu, L.N. Wang, J.X. Yu, X.X. Xu, Liberating photocarriers in mesoporous single-crystalline SrTaO₂N for efficient solar water splitting, Appl. Catal. B-Environ. 304 (2022), 120934, https://doi.org/10.1016/J.Apcatb.2021.120934.

[7] X.H. Wang, X.H. Wang, W.L. Tian, A. Meng, Z.J. Li, S.X. Li, L. Wang, G.C. Li, High-energy ball-milling constructing P-doped g-C₃N₄/MoP heterojunction with Mo-N bond bridged interface and Schottky barrier for enhanced photocatalytic H₂ evolution, Appl. Catal. B-Environ. 303 (2022), 120933, https://doi.org/10.1016/J.Apcatb.2021.120933.

[8] M. Zhang, X. Xin, Y.Q. Feng, J.H. Zhang, H. Lv, G.Y. Yang, Coupling Ni-substituted polyoxometalate catalysts with water-soluble CdSe quantum dots for ultraefficient photogeneration of hydrogen under visible light, Appl. Catal. B-Environ. 303 (2022), 120893, https://doi.org/10.1016/J.Apcatb.2021.120893.

[9] K. Das, R. Bariki, D. Majhi, A. Mishra, K.K. Das, R. Dhiman, B.G. Mishra, Facile synthesis and application of CdS/Bi₂₀TiO₃₂/Bi₄Ti₃O₁₂ ternary heterostructure: a synergistic multi-heterojunction photocatalyst for enhanced endosulfan degradation and hydrogen evolution reaction, Appl. Catal. B-Environ. 303 (2022), 120902, https://doi.org/10.1016/J.Apcatb.2021.120902.

[10] S. Liu, X.Y. Guo, W.J. Wang, Y. Yang, C.T. Zhu, C.Y. Li, W.H. Lin, Q.H. Tian, Y. Liu, CdS-Cu₁.₈₁S heteronanorods with continuous sublattice for photocatalytic hydrogen production, Appl. Catal. B-Environ. 303 (2022), 120909, https://doi.org/10.1016/J.Apcatb.2021.120909.

[11] H. Kato, K. Asakura, A. Kudo, Highly efficient water splitting into H₂ and O₂ over lanthanum-doped NaTaO₃ photocatalysts with high crystallinity and surface nanostructure, J. Am. Chem. Soc. 125 (2003) 3082–3089, https://doi.org/10.1021/ja027751g.

[12] S.S. Chen, T. Takata, K. Domen, Particulate photocatalysts for overall water splitting, Nat. Rev. Mater. 2 (2017) 17050, https://doi.org/10.1038/natrevmats.2017.50.

[13] K. Takanabe, Photocatalytic water splitting: quantitative approaches toward photocatalyst by design, ACS Catal. 7 (2017) 8006–8022, https://doi.org/10.1021/acscatal.7b02662.

[14] A. Kasahara, K. Nukumizu, G. Hitoki, T. Takata, J.N. Kondo, M. Hara, H. Kobayashi, K. Domen, Photoreactions on LaTiO₂N under visible light irradiation, J. Phys. Chem. A 106 (2002) 6750–6753, https://doi.org/10.1021/jp025961.

[15] F.X. Zhang, A. Yamakata, K. Maeda, Y. Moriya, T. Takata, J. Kubota, K. Teshima, S. Oishi, K. Domen, Cobalt-modified porous single-crystalline LaTiO₂N for highly efficient water oxidation under visible light, J. Am. Chem. Soc. 134 (2012) 8348–8351, doi:10.1021/ja301726c.

[16] A.E. Maegli, E.H. Otal, T. Hisatomi, S. Yoon, C.M. Leroy, N. Schauble, Y. Lu, M. Gratzel, A. Weidenkaff, Perovskite-type LaTiO2N oxynitrides for solar water splitting: influence of the synthesis conditions. Emrs Symposium T: Materials for Solar Hydrogen Via Photo-Electrochemical Production 22 (2012) 61–66. doi: 10.1016/j.egypro.2012.05.218.

[17] D. Logvinovich, L. Bocher, D. Sheptyakov, R. Figi, S.G. Ebbinghaus, R. Aguiar, M. H. Aguirre, A. Reller, A. Weidenkaff, Microstructure, surface composition and chemical stability of partly ordered LaTiO₂N, Solid State Sci. 11 (2009) 1513–1519, https://doi.org/10.1016/j.solidstatesciences.2009.05.024.

[18] A. Kasahara, K. Nukumizu, T. Takata, J.N. Kondo, M. Hara, H. Kobayashi, K. Domen, LaTiO₂N as a visible-light (≤600 nm)-driven photocatalyst (2), J. Phys. Chem. B 107 (2003) 791–797, https://doi.org/10.1021/jp026767q.

[19] D. Logvinovich, A. Borger, M. Dobeli, S.G. Ebbinghaus, A. Reller, A. Weidenkaff, Synthesis and physical chemical properties of Ca-substituted LaTiO₂N, Prog. Solid State Chem. 35 (2007) 281–290, https://doi.org/10.1016/j.progsolidstchem.2007.01.006.

[20] G.A. Lin, X.X. Xu, Ba-modified LaTiO₂N as an efficient visible light active photocatalyst for water oxidation, ACS Sustain. Chem. Eng. 8 (2020) 9641–9649, https://doi.org/10.1021/acssuschemeng.0c00302.

[21] F.F. Wu, G. Liu, X.X. Xu, Efficient photocatalytic oxygen production over Ca-modified LaTiO₂N, J. Catal. 346 (2017) 10–20, https://doi.org/10.1016/j.jcat.2016.11.022.

[22] M. Matsukawa, R. Ishikawa, T. Hisatomi, Y. Moriya, N. Shibata, J. Kubota, Y. Ikuhara, K. Domen, Enhancing photocatalytic activity of LaTiO₂N by removal of surface reconstruction layer, Nano Lett. 14 (2014) 1038–1041, https://doi.org/10.1021/nl404688h.

[23] R. Aguiar, D. Logvinovich, A. Weidenkaff, A. Reller, S.G. Ebbinghaus, Thermal oxidation of oxynitride perovskites in different atmospheres, Thermochim. Acta 471 (2008) 55–60, https://doi.org/10.1016/j.tca.2008.02.021.

[24] A.E. Maegli, T. Hisatomi, E.H. Otal, S. Yoon, S. Pokrant, M. Gratzel, A. Weidenkaff, Structural and photocatalytic properties of perovskite-type (La,Ca)Ti(O,N)₃ prepared from A-site deficient precursors, J. Mater. Chem. 22 (2012) 17906–17913, https://doi.org/10.1039/c2jm32718j.

[25] F. Chevire, F. Tessier, R. Marchand, Optical properties of the perovskite solid solution LaTiO₂N-ATiO₃ (A = Sr, Ba), Eur. J. Inorg. Chem. (2006) 1223–1230, https://doi.org/10.1002/ejic.200500743.

[26] C.S. Pan, T. Takata, M. Nakabayashi, T. Matsumoto, N. Shibata, Y. Ikuhara, K. Domen, A complex perovskite-type oxynitride: the first photocatalyst for water splitting operable at up to 600 nm, Angew. Chem. Int. Ed. 54 (2015) 2955–2959, https://doi.org/10.1002/anie.201410961.

[27] J.Y. Cui, Y. Qi, B.B. Dong, L.C. Mu, Q. Ding, G. Liu, M.J. Jia, F.X. Zhang, C. Li, One-pot synthesis of BaMg₁/₃Ta₂/₃O₃₋ₓNᵧ/Ta₃N₅ heterostructures as H₂-evolving photocatalysts for construction of visible-light-driven Z-scheme overall water splitting, Appl. Catal. B-Environ. 241 (2019) 1–7, https://doi.org/10.1016/j.apcatb.2018.09.014.

[28] X.Q. Sun, G. Liu, X.X. Xu, Defect management and efficient photocatalytic water oxidation reaction over Mg modified SrNbO₂N, J. Mater. Chem. A 6 (2018) 10947–10957, https://doi.org/10.1039/c8ta00767e.

[29] Y.W. Wang, S. Jin, X.Q. Sun, S.H. Wei, L. Chen, X.X. Xu, Switching on efficient photocatalytic water oxidation reactions over CaNbO₂N by Mg modifications under visible light illumination, Appl. Catal. B-Environ. 245 (2019) 10–19, https://doi.org/10.1016/j.apcatb.2018.12.033.

[30] S.S. Chen, S. Shen, G.J. Liu, Y. Qi, F.X. Zhang, C. Li, Interface engineering of a CoOₓ/Ta₃N₅ photocatalyst for unprecedented water oxidation performance under visible-light-irradiation, Angew. Chem. Int. Ed. 54 (2015) 3047–3051, https://doi.org/10.1002/anie.201409906.

[31] J.D. Xiao, J.J.M. Vequizo, T. Hisatomi, J. Rabeah, M. Nakabayashi, Z. Wang, Q. Xiao, H.H. Li, Z.H. Pan, M. Krause, N. Yin, G. Smith, N. Shibata, A. Bruckner, A. Yamakata, T. Takata, K. Domen, Simultaneously tuning the defects and surface properties of Ta3N5 nanoparticles by Mg-Zr codoping for significantly accelerated photocatalytic H-2 evolution, J. Am. Chem. Soc. 143 (2021) 10059–10064, https://doi.org/10.1021/jacs.1c04861.

[32] S. Ikeda, M. Hara, J.N. Kondo, K. Domen, H. Takahashi, T. Okubo, M. Kakihana, Preparation of K₂La₂Ti₃O₁₀ by polymerized complex method and photocatalytic decomposition of water, Chem. Mater. 10 (1998) 72–77, https://doi.org/10.1021/cm970221c.

[33] S.F. Chang, J.X. Yu, R. Wang, Q.Y. Fu, X.X. Xu, LaTaON₂ mesoporous single crystals for efficient photocatalytic water oxidation and Z-scheme overall water splitting, ACS Nano 15 (2021) 18153–18162, https://doi.org/10.1021/acsnano.1c06871.

[34] Y.W. Wang, S. Jin, G.X. Pan, Z.X. Li, L. Chen, G. Liu, X.X. Xu, Zr doped mesoporous LaTaON₂ for efficient photocatalytic water splitting, J. Mater. Chem. A 7 (2019) 5702–5711, https://doi.org/10.1039/c8ta11561c.

[35] A. Petala, A. Noe, Z. Frontistis, C. Drivas, S. Kennou, D. Mantzavinos, D. I. Kondarides, Synthesis and characterization of CoOₓ/BiVO₄ photocatalysts for the degradation of propyl paraben, J. Hazard. Mater. 372 (2019) 52–60, https://doi.org/10.1016/j.jhazmat.2018.03.008.

[36] S.H. Wei, S.F. Chang, F. Yang, Z.P. Fu, G. Liu, X.X. Xu, Stable and efficient solar-driven photoelectrochemical water splitting into H₂ and O₂ based on a BaTaO₂N photoanode decorated with CoO microflowers dagger, Chem. Commun. (2021), https://doi.org/10.1039/d0cc07778j.

[37] E.B. Hua, S. Jin, X.R. Wang, S. Ni, G. Liu, X.X. Xu, Ultrathin 2D type-II p-n heterojunction La₂Ti₂O₇/In₂S₃ with efficient charge separations and photocatalytic

hydrogen evolution under visible light illumination, Appl. Catal. B-Environ. 245 (2019) 733–742, https://doi.org/10.1016/j.apcatb.2019.01.024.

[38] L. Yang, J.X. Yu, Q.Y. Fu, L.L. Kong, X.X. Xu, Mesoporous single-crystalline SrNbO$_2$N: expediting charge transportation to advance solar water splitting, Nano Energy 95 (2022), 107059, https://doi.org/10.1016/j.nanoen.2022.107059.

[39] M. Yashima, M. Saito, H. Nakano, T. Takata, K. Ogisu, K. Domen, Imma perovskite-type oxynitride LaTiO$_2$N: structure and electron density, Chem. Commun. 46 (2010) 4704–4706, https://doi.org/10.1039/c0cc00573h.

[40] I. Levin, T.A. Vanderah, T.G. Amos, J.E. Maslar, Structural behavior and Raman spectra of perovskite-like solid solutions (1-x)LaMg$_{0.5}$Ti$_{0.5}$O$_3$-xLa$_{2/3}$TiO$_3$, Chem. Mater. 17 (2005) 3273–3280, https://doi.org/10.1021/cm040389f.

[41] M. Avdeev, M.P. Seabra, V.M. Ferreira, Crystal structure of dielectric ceramics in the La(Mg$_{0.5}$Ti$_{0.5}$)O$_3$-BaTiO$_3$ system, J. Mater. Res. 17 (2002) 1112–1117, doi: 10.1557/Jmr.2002.0164.

[42] Y.I. Kim, P.M. Woodward, Syntheses and characterizations of complex perovskite oxynitrides LaMg$_{1/3}$Ta$_{2/3}$O$_2$N, LaMg$_{1/2}$Ta$_{1/2}$O$_{5/2}$N$_{1/2}$, and BaSc$_{0.05}$Ta$_{0.95}$O$_{2.1}$N$_{0.9}$, J. Solid State Chem. 180 (2007) 3224–3233, https://doi.org/10.1016/j.jssc.2007.08.031.

[43] M.L. Lv, S. Ni, Z. Wang, T.C. Cao, X.X. Xu, Cation ordering/disordering effects upon photocatalytic activity of CrNbO$_4$, CrTaO$_4$, Sr$_2$CrNbO$_6$ and Sr$_2$CrTaO$_6$, Int. J. Hydrog. Energy 41 (2016) 1550–1558, https://doi.org/10.1016/j.ijhydene.2015.11.057.

[44] H.W. Eng, P.W. Barnes, B.M. Auer, P.M. Woodward, Investigations of the electronic structure of d(0) transition metal oxides belonging to the perovskite family, J. Solid State Chem. 175 (2003) 94–109, https://doi.org/10.1016/S0022-4596(03)00289-5.

[45] B. Moss, Q. Wang, K.T. Butler, R. Grau-Crespo, S. Selim, A. Regoutz, T. Hisatomi, R. Godin, D.J. Payne, A. Kafizas, K. Domen, L. Steier, J.R. Durrant, Linking in situ charge accumulation to electronic structure in doped SrTiO$_3$ reveals design principles for hydrogen-evolving photocatalysts, Nat. Mater. 20 (2021) 511–517, https://doi.org/10.1038/s41563-020-00868-2.

[46] B. Siritanaratkul, K. Maeda, T. Hisatomi, K. Domen, Synthesis and photocatalytic activity of perovskite niobium oxynitrides with wide visible-light absorption bands, ChemSusChem 4 (2011) 74–78, https://doi.org/10.1002/cssc.201000207.

[47] Y.Q. Xiao, C. Feng, J. Fu, F.Z. Wang, C.L. Li, V.F. Kunzelmann, C.M. Jiang, M. Nakabayashi, N. Shibata, I.D. Sharp, K. Domen, Y.B. Li, Band structure engineering and defect control of Ta$_3$N$_5$ for efficient photoelectrochemical water oxidation, Nat. Catal. 3 (2020) 932–940, https://doi.org/10.1038/s41929-020-00522-9.

[48] S.H. Wei, G. Zhang, X.X. Xu, Activating BaTaO$_2$N by Ca modifications and cobalt oxide for visible light photocatalytic water oxidation reactions, Appl. Catal. B-Environ. 237 (2018) 373–381, https://doi.org/10.1016/j.apcatb.2018.06.017.

[49] P.A. Cox, The Electronic Structure and Chemistry of Solids, Oxford University Press, 1987.

[50] Y.W. Wang, S.H. Wei, X.X. Xu, SrTaO$_2$N-CaTaO$_2$N solid solutions as efficient visible light active photocatalysts for water oxidation and reduction, Appl. Catal. B-Environ. 263 (2020), 118315, https://doi.org/10.1016/J.Apcatb.2019.118315.

[51] X.Q. Sun, Y.L. Mi, F. Jiao, X.X. Xu, Activating layered perovskite compound Sr$_2$TiO$_4$ via La/N codoping for visible light photocatalytic water splitting, ACS Catal. 8 (2018) 3209–3221, https://doi.org/10.1021/acscatal.8b00369.

[52] M.A. Fox, M.T. Dulay, Heterogeneous photocatalysis, Chem. Rev. 93 (1993) 341–357, https://doi.org/10.1021/cr00017a016.

[53] M.R. Hoffmann, S.T. Martin, W.Y. Choi, D.W. Bahnemann, Environmental applications of semiconductor photocatalysis, Chem. Rev. 95 (1995) 69–96, https://doi.org/10.1021/cr00033a004.

[54] J.L. Du, Z.F. Chen, C.C. Chen, T.J. Meyer, A half-reaction alternative to water oxidation: chloride oxidation to chlorine catalyzed by silver ion, J. Am. Chem. Soc. 137 (2015) 3193–3196, https://doi.org/10.1021/jacs.5b00037.

[55] B.H. Meekins, P.V. Kamat, Got TiO$_2$ nanotubes? Lithium ion intercalation can boost their photoelectrochemical performance, ACS Nano 3 (2009) 3437–3446, https://doi.org/10.1021/nn900897r.

[56] Y.H. Xie, Y.W. Wang, Z.F. Chen, X.X. Xu, Role of oxygen defects on the photocatalytic properties of Mg-doped mesoporous Ta$_3$N$_5$, ChemSusChem 9 (2016) 1403–1412, https://doi.org/10.1002/cssc.201600193.

[57] M. Anpo, M. Che, Applications of photoluminescence techniques to the characterization of solid surfaces in relation to adsorption, catalysis, and photocatalysis, Adv. Catal. 44 (1999) 119–257, https://doi.org/10.1016/S0360-0564(08)60513-1.

[58] T.W. Kim, K.S. Choi, Nanoporous BiVO$_4$ photoanodes with dual-layer oxygen evolution catalysts for solar water splitting, Science 343 (2014) 990–994, https://doi.org/10.1126/science.1246913.

[59] Y.J. Zhong, Z.S. Li, X. Zhao, T. Fang, H.T. Huang, Q.F. Qian, X.F. Chang, P. Wang, S.C. Yan, Z.T. Yu, Z.G. Zou, Enhanced water-splitting performance of perovskite SrTaO$_2$N photoanode film through ameliorating interparticle charge transport, Adv. Funct. Mater. 26 (2016) 7156–7163, https://doi.org/10.1002/adfm.201603021.

[60] T. Rajh, A.E. Ostafin, O.I. Micic, D.M. Tiede, M.C. Thurnauer, Surface modification of small particle TiO$_2$ colloids with cysteine for enhanced photochemical reduction: an EPR, Study J. Phys. Chem. 100 (1996) 4538–4545, doi:10.1021/jp952002p.

[61] S. Livraghi, M. Chiesa, M.C. Paganini, E. Giamello, On the nature of reduced states in titanium dioxide as monitored by electron paramagnetic resonance. I: the anatase case, J. Phys. Chem. C 115 (2011) 25413–25421, https://doi.org/10.1021/jp209075m.

[62] A. Yamakata, M. Kawaguchi, N. Nishimura, T. Minegishi, J. Kubota, K. Domen, Behavior and energy states of photogenerated charge carriers on Pt- or CoO$_x$-loaded LaTiO$_2$N photocatalysts: time-resolved visible to mid-infrared absorption study, J. Phys. Chem. C 118 (2014) 23897–23906, https://doi.org/10.1021/jp508233z.

[63] S.M. Prokes, J.L. Gole, X.B. Chen, C. Burda, W.E. Carlos, Defect-related optical behavior in surface-modified TiO$_2$ nanostructures, Adv. Funct. Mater. 15 (2005) 161–167, https://doi.org/10.1002/adfm.200305109.

[64] H. Xiao, J. Tahir-Kheli, W.A. Goddard, Accurate band gaps for semiconductors from density functional theory, J. Phys. Chem. Lett. 2 (2011) 212–217, doi: 10.1021/Jz101565j.

[65] B.A. Pinaud, Z.B. Chen, D.N. Abram, T.F. Jaramillo, Thin films of sodium birnessite-type MnO$_2$: optical properties, electronic band structure, and solar photoelectrochemistry, J. Phys. Chem. C 115 (2011) 11830–11838, https://doi.org/10.1021/jp200015p.

[66] Y. Matsumoto, Energy positions of oxide semiconductors and photocatalysis with iron complex oxides, J. Solid State Chem. 126 (1996) 227–234, doi:10.1006/jssc.1996.0333.